A microrobotic platform actuated by thermocapillary flows for manipulation at the air-water interface

Franco Nicolas Pinan Basualdo, Aude Bolopion, Michaël Gauthier, Pierre Lambert

A Microrobotic Platform Actuated by Thermocapillary Flows for Manipulation at the Air-Water Interface

Franco N. Piñan Basualdo,[1,2*] A. Bolopion,[2] M. Gauthier,[2] P. Lambert [1]

[1]Transfers Interfaces and Processes (TIPs), Ecole Polytechnique de Bruxelles (CP 165/67),
Université Libre de Bruxelles, 1050 Brussels, Belgium
[2]FEMTO-ST Institute, CNRS, Univ. Bourgogne Franche-Comté,
24 rue Savary, F-25000 Besançon, France
*To whom correspondence should be addressed: E-mail: Franco.Pinan.Basualdo@ulb.be

Future developments in micromanufacturing will require advances in micromanipulation tools. Several robotic micromanipulation methods have been developed to position micro-objects mostly in air and in liquids. The air-water interface is a third media where objects can be manipulated offering a good compromise between the two previously mentioned ones. Indeed, objects at the interface are not subjected to stick-slip due to dry friction in air, and profit from a reduced drag compared to those in water. Here, we present the ThermoBot, a microrobotic platform dedicated to the manipulation of objects placed at the air-water interface. For actuation, ThermoBot uses a laser-induced thermocapillary flow, which arises from the surface stress caused by the temperature gradient at the fluid interface. The actuated objects can reach velocities up to ten times their body length per second without any on-board actuator. Moreover, the localized nature of the thermocapillary flow enables the simultaneous and independent control of multiple objects, thus paving the way for microassembly operations at the air-water interface. We demonstrate that our setup can be used to direct capillary-based self-assemblies at this interface. We illustrate the ThermoBot's capabilities through three examples: simultaneous control of up to four spheres, control of complex objects in both position and orientation, and directed self-assembly of multiple pieces.

ThermoBot: using a laser-induced thermocapillary flow to manipulate floating micro-objects and assist self-assembly.

Introduction

Most of the research aiming to develop microrobotic platforms target two main media: air and liquid. However, microrobotic tools have recently been developed to work at the air-water interface (*1–4*). Micromanipulation at the interface profits from a reduced drag compared to the liquid bulk, and it is not subjected to dry friction inducing the stick-slip motion usually seen in dry environments (*5*). Moreover, at submillimetric scales, surface tension becomes substantial, for instance allowing objects denser than water to float. In this article, we therefore propose the ThermoBot: a non-contact manipulation platform working at the air-water interface and based on surface tension effects. The proposed setup can be used to stimulate the self-assembly (*6*) of floating objects, thereby paving the way for the development of micromanufacturing operations at the air-water interface.

Different actuation methods have been developed at the air-water interface, among which rower robots, magnetic actuation, and surface tension based actuation are the most common ones. Rower robots, inspired by insects, use the drag force to propel themselves (*7–10*). This kind of robots can easily be controlled but the actuators must be placed on the floating robots themselves, making them complex to miniaturize below the centimeter scale. To avoid having to use embedded actuators, the most common alternative is magnetic actuation by an externally controlled magnetic field. Magnetic actuation has been proven to allow a precise position control at the air-water interface (*1, 5, 11, 12*), but it requires materials with specific magnetic properties. Additionally, magnetic actuation is adequate to control swarms where all agents are subjected to similar actuation forces, but the multi-object control is challenging since all the agents are affected by the same magnetic field. Recently, researchers have achieved magnetic multi-object control, using additional physical effects (*13*), the different dynamic response of the agents (*14*) or spatially selective actuation (*15*). The third actuation option at the air-water interface is to directly exploit the surface tension, a substantial effect at the microscale.

Surface tension is a property of the interface (here the air-water interface) that can be considered an excess of energy at the surface (*16*), making the interface behave similarly to an elastic membrane. Therefore, interfaces develop a restoring force when deformed by an object, making it possible for objects denser than water to float (*17*). Furthermore, in the presence of a gradient of surface tension, low surface tension areas (low excess energy) tend to expand towards high surface tension areas (minimizing the excess energy), thereby giving rise to convective flows. This effect, known as Marangoni effect (*18*), can be used to propel floating objects through a surface tension gradient. One option to generate such a gradient is to locally decrease the surface tension using solvents or surfactants (solutocapillary actuation), as some insects do to rapidly escape predators (*19*). This technique is appealing since it induces high speeds (*2, 4, 20–23*) and does not require any external source of energy. However, increasing the lifespan is challenging due to fuel depletion and surface saturation. The control of the propulsion direction requires additional physical effects. Another option is to locally decrease the surface tension by heating the air-water interface (thermocapillary actuation), thereby generating a convective flow at the interface from hot to cold areas. This effect has already been exploited to manipulate

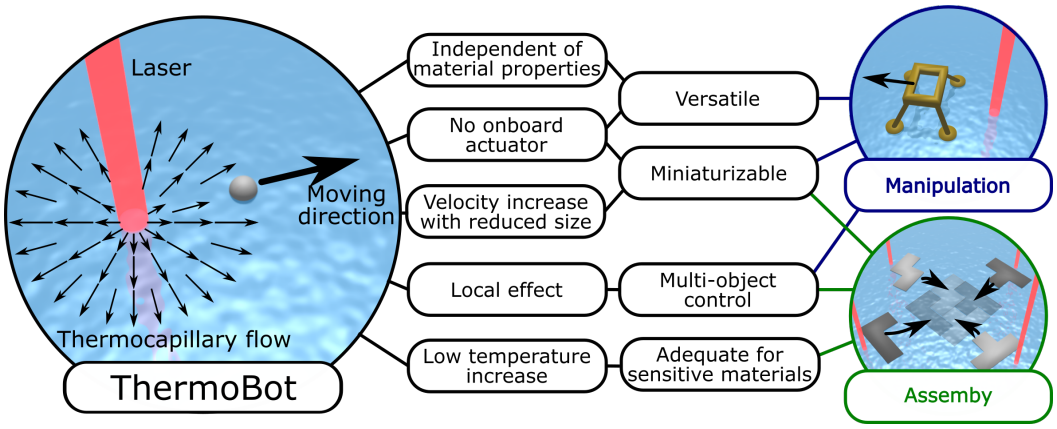

Figure 1: Sketch and diagram showing the **ThermoBot's** main characteristics. ThermoBot constitutes a new micromanipulation tool and paves the way for new micromanufacturing operations at the air-water interface

bubbles (*24*) and cells (*25*) in the liquid bulk, and droplets (*26*) and solid spheres (*27*) at the interface. We demonstrate that this physical effect can also be used to control objects placed at the interface in both position and orientation, opening the possibility for the development of a microrobotic platform able to perform microassembly operations.

In this paper, we present ThermoBot: a microrobotic platform using thermocapillary actuation to manipulate objects at the air-water interface. The thermocapillary flow is generated by heating the air-water interface with an infrared laser, thereby conveying the floating objects away from the laser spot. The objects are then controlled by displacing the laser spot around them. Since the objects are propelled by the flow, they can be of any shape and material as long as they float. The attained velocities are only surpassed by those of solutocapillary-based actuation (Fig. S1); however, ThermoBot allows us to control the displacement direction, among other advantages (Table S1). The ThermoBot's actuation principle offers a promising route for a robotic platform enabling micromanufacturing operations at the air-water interface (Fig. 1). At this interface, lateral capillary forces (*28, 29*) enable the self-assembly of floating objects (*12, 30, 31*); therefore, we propose ThermoBot as a way to actively control such assemblies. ThermoBot does not only speed up the self-assembly or prevent defaults, but also allows us to purposely drive the system to a metastable assembly. Based on an accurate knowledge of the ThermoBot actuation principle, we demonstrate experimentally the following capabilities: simultaneous control of multiple spheres, control of a multiple-legged object in both position and orientation, and directed self-assembly.

Results

ThermoBot actuation system

ThermoBot actuates floating objects through a laser-induced thermocapillary flow. The actuation system consists in pointing an infrared laser beam at a water volume whose top surface is in contact with air (Fig. 2A). The water will absorb the laser energy which locally increases the temperature (T) and, due to the surface tension (σ) variation with temperature (Fig. S2A), decreases the surface tension. Thanks to the Marangoni effect (*18*), this surface tension gradient creates a convective flow, known as thermocapillary flow. This effect can be conceptually understood by considering a volume of fluid just below the interface that, due to the surface tension gradient, will undergo a net attraction towards high surface tension (i.e. colder) regions. This force is balanced by the shear stress with lower fluid layers, and this equilibrium is written mathematically as:

$$\mu \frac{\partial \mathbf{U}}{\partial \mathbf{n}} = -\nabla_{\mathbf{S}} \sigma = -\frac{\partial \sigma}{\partial T} \nabla_{\mathbf{S}} T \,, \tag{1}$$

where $\mathbf{U}$ is the fluid velocity vector, $\mathbf{n}$ a unit vector normal to the interface that points down towards the water phase, μ the fluid's dynamic viscosity and $\nabla_{\mathbf{S}}$ the surface gradient operator ($\nabla_{\mathbf{S}} f = \nabla f - \mathbf{n}(\mathbf{n} \cdot \nabla f)$). In the temperature range within which we are operating, we can consider a constant value $\partial\sigma/\partial T \approx -155\,\mu\mathrm{N}/(\mathrm{m\,K})$ (Fig. S2A). In our setup, we use an infrared laser (wavelength $\lambda = 1455\,\mathrm{nm}$) that is collimated to obtain a $1.3\,\mathrm{mm}$ diameter spot at the interface. The main advantage of using a laser as an energy source is that even with a moderate laser power (up to $150\,\mathrm{mW}$), we obtain a high power density (up to $250\,\mathrm{mW/mm^2}$) compared to other heating mechanisms. We performed numerical simulations of the flow (Supplementary Material B) and observed that the generated flow is a toroidal convection cell around the laser spot (Fig. 2B). The high power density of the laser generates high temperature gradients (up to $3500\,\mathrm{K/m}$), leading to high fluid velocities (up to $60\,\mathrm{mm/s}$), with relatively small temperature increases (peak temperature up to $5\,\mathrm{K}$) (Fig. 2C). Notice that the laser power is low compared to the total heat capacity of the water volume (average temperature increase limited to $70\,\mathrm{mK/min}$). Once onset, this thermocapillary flow conveys floating objects away from the laser spot. The laser range (radius of the area affected by the flow) was also estimated trough simulations and measured experimentally (Fig. 2D). It was observed to vary from $3\,\mathrm{mm}$ for a laser power of $20\,\mathrm{mW}$ to $9\,\mathrm{mm}$ for a laser power of $150\,\mathrm{mW}$. Therefore, even though increasing the laser power would increase the effect, it would also increase the area affected by the laser, thus making it harder to independently control multiple objects.

The actuation system is completed by a piezoelectric tip/tilt mirror capable of steering the laser spot on the interface, and a camera used to close the control loop (Fig. 2A). The mirror rotation limits and its distance to the interface result in a $80 \times 80\,\mathrm{mm^2}$ workspace, while its fast dynamics (response time around $2\,\mathrm{ms}$) allow the multiplexing of the laser beam (Supplementary Material C), to simultaneously control multiple objects or to use multiple laser spots to control a complex object. We use the laser spot position as the control variable, allowing us to perform

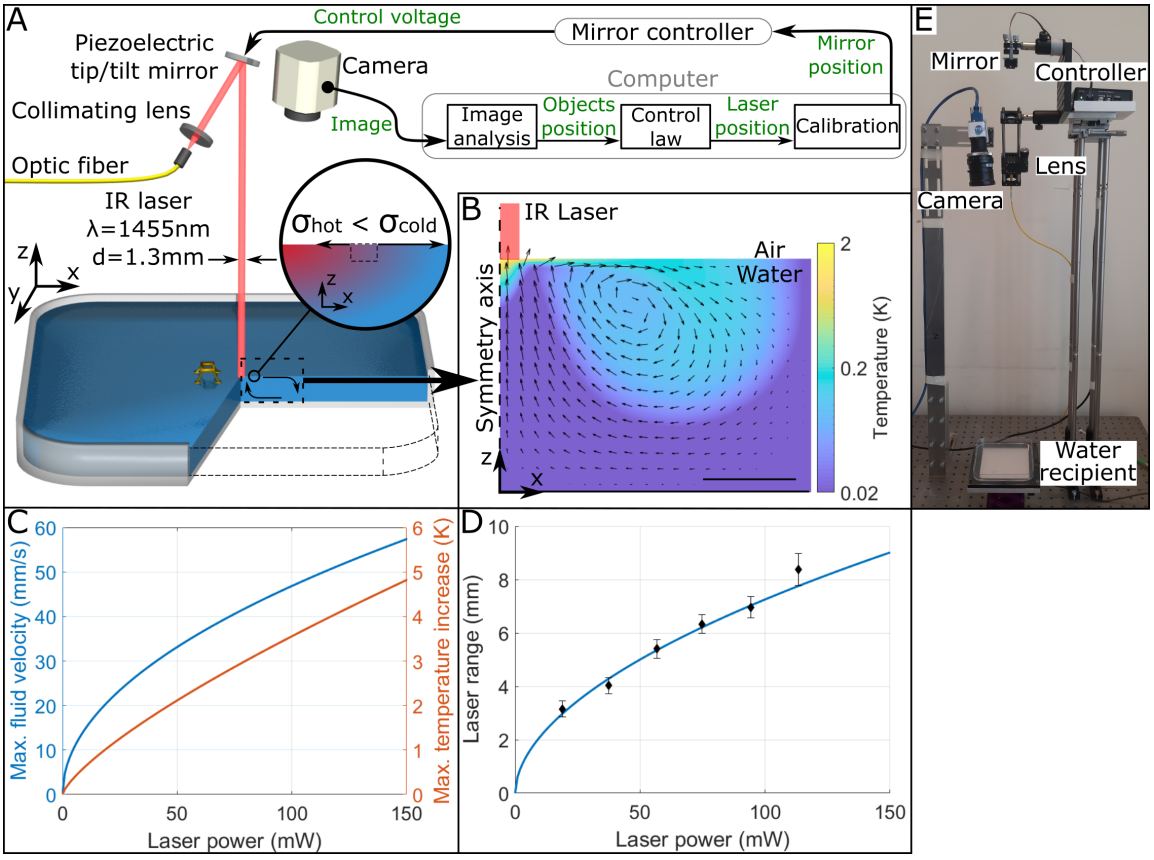

Figure 2: **ThermoBot microrobotic platform.** **(A)** Schematics of system control loop from image acquisition to mirror control and the laser-induced thermocapillary effect. For animation, see movie S1. **(B)** Flow simulation results for a laser power of $50\,\mathrm{mW}$. The color map represents the temperature, and the arrows represent the flow velocity (both are in logarithmic scales since the values at the surface are much higher than in the bulk). Scale bar $3\,\mathrm{mm}$. **(C)** Flow simulation results: maximum temperature increase (at the interface and at the center of the laser beam) and maximum fluid velocity (at the interface and at around $1\,\mathrm{mm}$ from the laser beam) as a function of the laser power. **(D)** Range of the laser effect: flow simulations results (see Supplementary Material B for more details) and measurements performed by spreading aluminum flakes (typical size of $70\,\mu\mathrm{m}$ on the interface and measuring how far they are repelled by the flow. The error bars represent the range (difference between highest and lowest value) of 3 measurements. **(E)**. Picture of the experimental setup.

complex operations without having to vary the laser power (although we do change the laser power between experiments).

Simultaneous control of multiple spheres

Firstly, we demonstrate the simultaneous and precise control of multiple spheres (Fig. 3A). In this experiment we displace $500\,\mu\mathrm{m}$ diameter steel spheres able to float at the air-water interface thanks to the surface tension (*17*). When the laser spot is kept at a constant distance from the sphere, the latter accelerates until reaching a steady velocity depending on the laser-sphere distance and on the laser power (Fig. 3B). By multiplexing the laser, we simultaneously steered two spheres along a closed path (Fig. 3D) using a self-developed closed loop path-following technique (Supplementary Material D). The technique successfully keeps the sphere on the path, with an error of up to $0.9\,\mathrm{mm}$ and a mean error of $0.2\,\mathrm{mm}$ after the initial approach (Fig. 3C). As another example of the ThermoBot's capabilities, four spheres were simultaneously controlled, first separating them, and then rotating them clockwise (Fig. 3E). In the last experiment, no path was prescribed, instead there was a moving target for each sphere.

Multiple-legged object control

Being able to multiplex the laser spot also enables the control of complex objects, such as a multiple-legged one (Fig. 4A). Although in this experiment the object is approximately 50 times heavier than the steel spheres, we can still obtain rotation and locomotion speeds of up to $80\,^\circ/\mathrm{s}$ and $8\,\mathrm{mm/s}$ respectively by using two laser spots (Fig. 4B). Based on these experiments, we developed a simple model (Fig S2) allowing us to estimate the robot's motion for any relative laser spot position. By placing each of the laser spots at a different distance from their leg, we could combine control of both translation and rotation of the object to make it follow a path (Fig. 4D). In this configuration, the robot's dynamics constitute a nonholonomic system (*32*) for which a controller was specifically developed (Supplementary Material E). ThermoBot made the objects follow the path with an error of up to $2.6\,\mathrm{mm}$ and a mean error of $1.2\,\mathrm{mm}$ (Fig. 4C).

Directed self-assembly

ThermoBot provides new ways of micromanufacturing at the air-water interface. Notably, it can be used to direct the self-assembly of objects at the interface, where the self-assembly is enabled by lateral capillary forces (Fig. 5A and 5B). Lateral capillary forces are interactions between floating objects (responsible for the clumping of breakfast cereals on the surface of a bowl of milk) which results from a minimization of surface and gravitational energy (*28, 29*). Although the capillary interactions can be tuned during the manufacturing of parts by adjusting their wetting properties (*30*) or their geometry (*31*), defects can still occur due to metastable states (local minimum energy configuration that is not the global minimum) and unfavorable initial positions. Moreover, since the strength of lateral capillary forces strongly decrease with

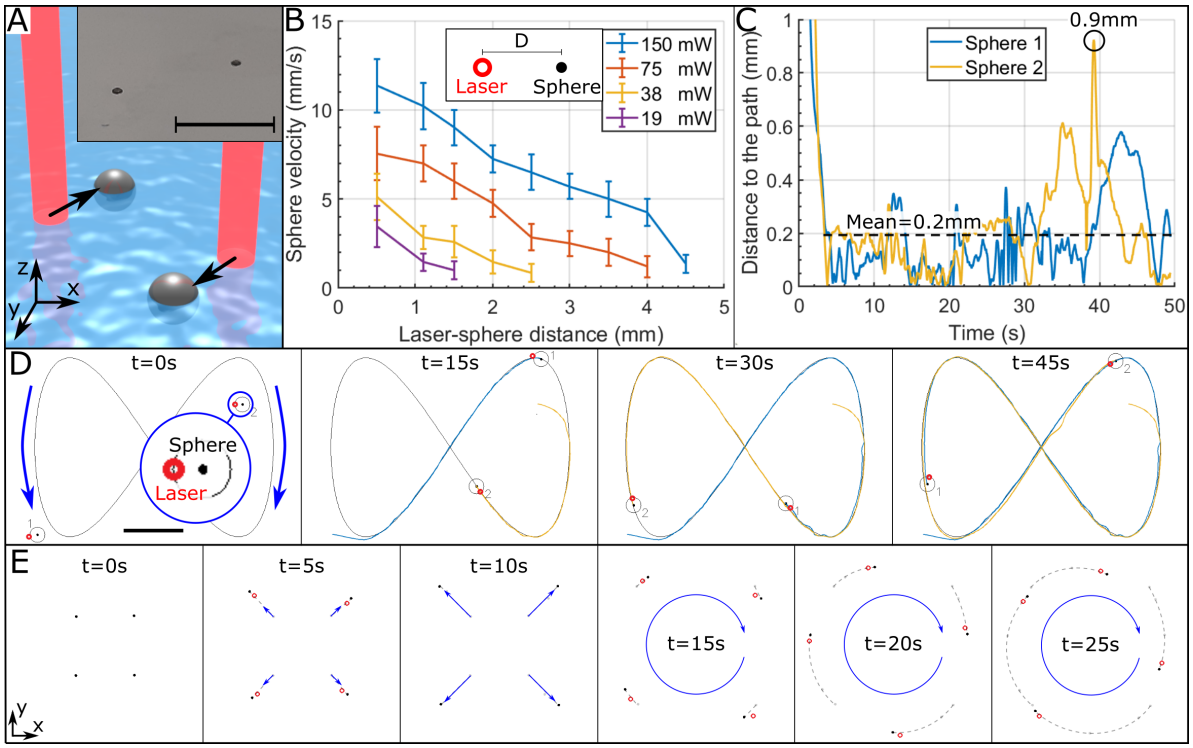

Figure 3: **Simultaneous control of multiple spheres.** **(A)** Schematics of two spheres being controlled independently. The inset is a picture of two spheres (scale bar $5\,\mathrm{mm}$). **(B)** Experimental characterization of sphere steady state velocity as a function of the laser-sphere distance and the laser power. The error bars represent the range (difference between highest and lowest value) of 8 measurements. **(C)** Experimental sphere-path distance evolution of the path-following experiment shown in D. **(D)** Experimental simultaneous control of two spheres following a path (Lissajous curve $x = 20\cos(\alpha)\,[\mathrm{mm}]$ and $y = 15\sin(2\alpha)\,[\mathrm{mm}]$ with $0 \leq \alpha < 2\pi$). A circle was added digitally around each of the spheres to make them easier to identify, the red circles represent the laser spots, and the blue and yellow lines represent the spheres' trajectories. Scale bar $10\,\mathrm{mm}$. See movie S2. **(E)** Experimental simultaneous control of four spheres. Same scale as D. See movie S3.

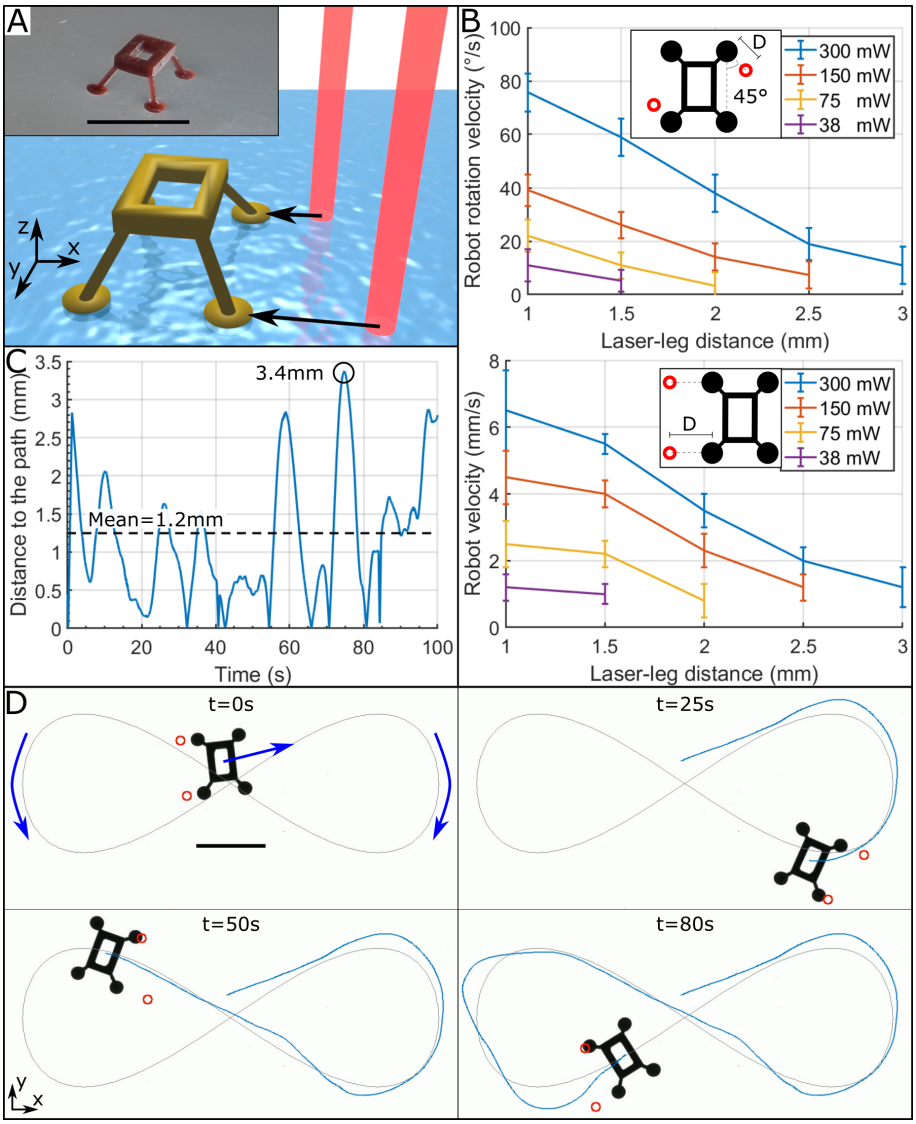

Figure 4: **Multiple-legged object control.** **(A)** Sketch of a floating object with four legs controlled by laser-induced thermocapillary flow. The inset is a picture of an object (scale bar $10\,\mathrm{mm}$). **(B)** Object rotation and displacement characterization as a function of the laser-leg distance and the total laser power. The error bars represent the range (difference between highest and lowest value) of 3 measurements. **(C)** Experimental robot-path distance evolution of the path-following experiment shown in D. **(D)** Experimental simultaneous orientation and position control of a four-legged object following a path (Lissajous curve $x = 30\sin(2\alpha)\,[\mathrm{mm}]$ and $y = 10\cos(\alpha)\,[\mathrm{mm}]$ with $0 < \alpha < 2\pi$). The red circles represent the laser spots, and the blue line represents the object trajectory. Scale bar $10\,\mathrm{mm}$. See movie S4.

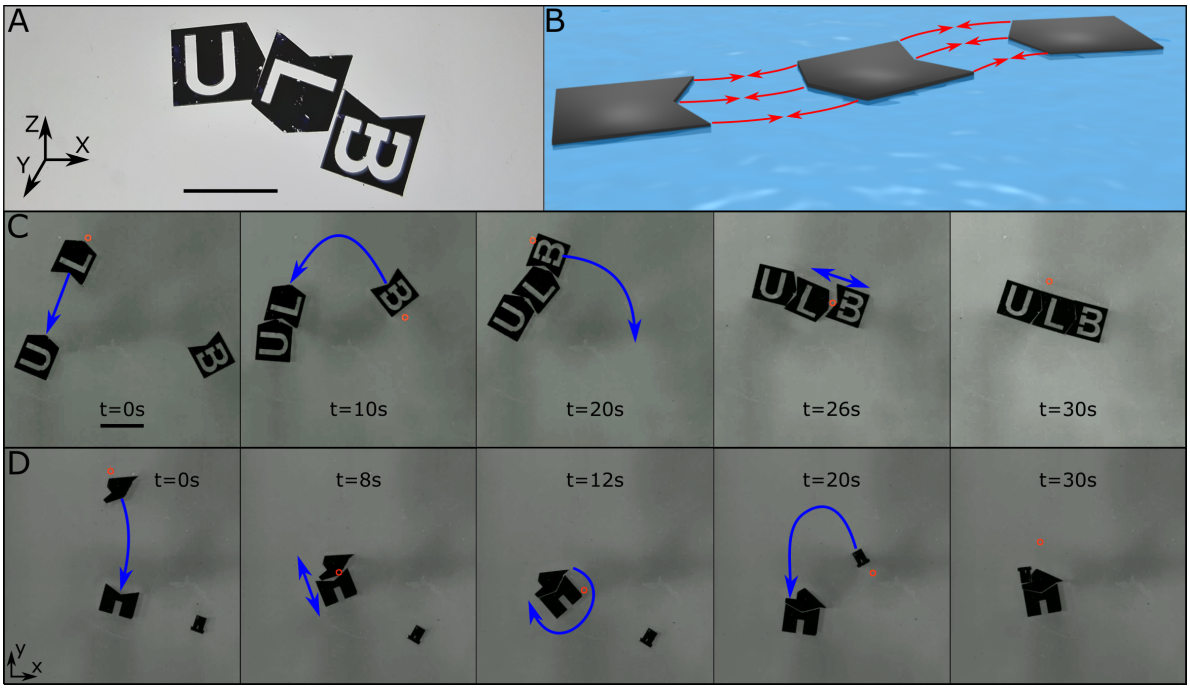

Figure 5: **Directed self-assembly.** **(A)** Picture of failed self-assembly (scale bar $10\,\mathrm{mm}$). **(B)** Schema of lateral capillary forces promoting self-assembly between pieces. **(C)** Experimental directed assembly of a U-L-B puzzle. The red circle represents the laser spot. Scale bar $10\,\mathrm{mm}$. See movie S5. **(D)** Experimental directed assembly of a house puzzle. Same scale as D. See movie S6.

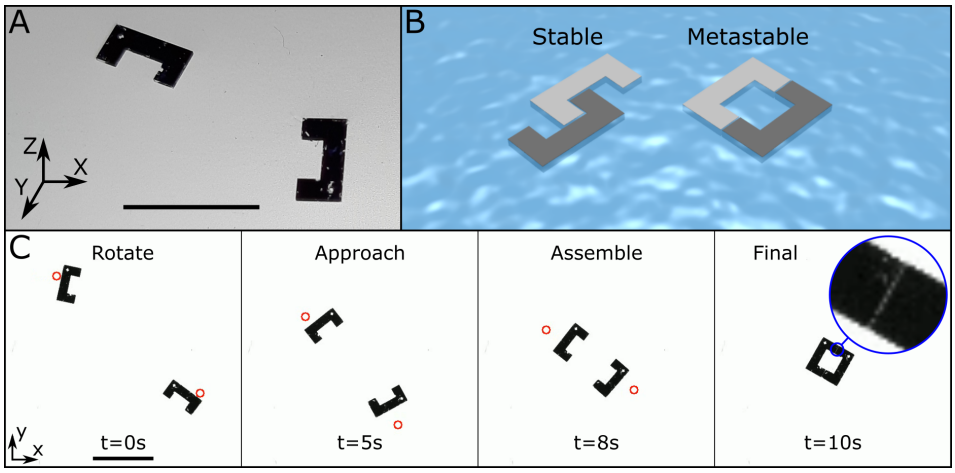

Figure 6: **Automatic metastable assembly of 'C' shape pieces. (A)** Picture of two 'C' shape pieces (scale bar 10 mm). **(B)** Schema showing a stable (left) and a metastable (right) assembly of two 'C' shape pieces. **(C)** Experimental automatic assembly of two 'C' shape pieces purposely driven to a metastable configuration. The red circles represent the laser spots. Scale bar 10 mm. See movie S7.

distance, if the parts are initially far apart, the initial approach can be slow. These problems can be solved adding active particles to the interface to direct the assembly (*12*), but these particles can also interfere with the assembly. Therefore, we propose to use ThermoBot to actively direct capillary-based self-assemblies, as it can be used to approach the parts with any desired orientation, preventing defects and speeding up the process. It can even rectify assembly defects by first separating the parts (Supplementary Material F) and then letting them re-assemble properly. Indeed, we successfully used ThermoBot to perform the self-assembly of a U-L-B (Fig. 5C) and a house-like (Fig. 5D) puzzles.

For some applications it might be interesting to drive the assembly to a metastable state, something that requires an active way to control the assembly. We have developed and automatic controller allowing us to purposely drive a system of two 'C' shape pieces to a metastable state (Fig. 6A and 6B) using ThermoBot. In this case an automatic controller was necessary since both particles are controlled simultaneously to approach each other with the desired orientation. The technique consists in rotating both particles to face one another and then approaching them towards each other. We repeated this experiment 31 times where the assembly failed only once. We attribute this failure to the fact that the particles were initially too close to each other for the controller to compensate the error in orientation. The results for the other 30 experiments are summarized in Table 1. This technique can easily be extended to assemble more pieces if they can be assembled in series (one piece added to the assembly at the time). However, it can be harder to implement when the simultaneous assembly of more than two pieces is needed, because the final approach is very fast and dominated by capillary forces, making it impossible to keep the orientation controlled.

Table 1: **Automatic metastable assembly results.** The error was measured normal to the line joining the two pieces by analyzing the images taken during the assembly (camera resolution of $80\,\mu\mathrm{m}$). The time was measured between the moment the algorithm was launched and the final assembly was achieved.

Error (μm)	[0, 100]	(100, 200]	(200, 300]
#N	24	5	1
Time (s)	[10, 20]	(20, 30]	$>$30
#N	23	5	2

Discussion

In this article we presented the ThermoBot, a microrobotic platform dedicated to the manipulation of objects placed at the air-water interface. The actuation system is based on the generation of a thermocapillary flow, a flow that arises from an interface temperature gradient thanks to the Marangoni effect (*18*). We generated this temperature gradient by pointing an infrared laser at the interface, which generated a flow that propelled floating objects away from the laser spot. By repositioning the laser spot using a piezoelectric tip/tilt mirror, we were able to control the object displacement. The laser's high power density allows the object to attain velocities of up to $12\,\mathrm{mm/s}$ ($24\,\mathrm{body\,lengths/s}$) with very low temperature increases (up to $5\,\mathrm{K}$), making our system suitable for actuating sensitive components, such as electronic components. Moreover, our system does not require any on-board actuators and it does not rely on any specific material properties, therefore making ThermoBot a highly versatile system. Furthermore, the localized nature of the thermocapillary flow enables the simultaneous and independent control of multiple objects. All these are the key features behind ThermoBot's capacity to perform controlled operations at the air-water interface. Notably, one of these operations is the direction of capillary-based self-assemblies, allowing to purposely drive the assembly to a metastable state and preventing defaults, hopefully paving the way for the emergence of micromanufacturing applications. It should also be noted that, since the objects' speed become independent of size at small scales, (theoretically, a massless point particle speed would be equal to the fluid velocity), scaling down the proposed setup could be an appealing actuation alternative at the micro and nanoscales.

In addition to the wide range of applications already presented in this article, we would like to mention further ways of exploiting our system's capabilities. With our current setup we were able to effectively multiplex the laser up to a maximum of five laser spots, this number limited mainly by the mirror speed. One way to further increase this number could be to make use of a spatial light modulator (*24*). This would not only allow us to increase the number of laser spots, but also to create an almost arbitrary illumination pattern, leading to complex flows and allowing the study of alternative control techniques.

Material and methods

ThermoBot's actuation system

Our setup can be subdivided into four different subsystems:

Optical system. We used an infrared (IR) laser source (Keopsys Fiber Raman Laser CRFL-01-1455-OM1-B130-FA) with a wavelength $\lambda = 1455\,\mathrm{nm}$ and an output power from $40\,\mathrm{mW}$ to $1\,\mathrm{W}$ to locally heat the water. The source output was connected using an optic fiber (Thorlabs SM980-5.8-125) to a fiber adapter (Thorlabs HAFC - FC/PC) in front of which we placed a collimating lens (Thorlabs Lens A110TM) with a focal length $f = 6.24\,\mathrm{mm}$. According to the supplier, the optic fiber mode field diameter for our wavelength is $\mathrm{MFD} = 8.8\,\mu\mathrm{m}$, obtaining an output beam diameter of $d \approx 4\lambda f/(\pi \mathrm{MFD}) = 1.3\,\mathrm{mm}$. The total efficiency of the optical system was measured to be around $50\,\%$, therefore the power reaching the interface can be varied between $20\,\mathrm{mW}$ and $500\,\mathrm{mW}$.

Mirror system. After being collimated, the laser beam reflected on a piezoelectric tip/tilt mirror (Mirrorcle A7M20.2-2000AL-DIP24-C/TP) which was located at approximately $80\,\mathrm{cm}$ from the interface. The mirror maximum rotation angles are $\pm 5°$, resulting in a maximum workspace of $140 \times 140\,\mathrm{mm}^2$ but we limited it to $80 \times 80\,\mathrm{mm}^2$ since the mirror behavior for high deflection angles is not linear. The mirror orientation was controlled by its own controller (Mirrorcle MEMS Controller USB-SL MZ) which was connected to the computer via USB. This controller generates the high voltage signals required to control the piezoelectric mirror and has an internal filter to protect the mirror from abrupt movements.

Water system. We used a $125 \times 125 \times 15\,\mathrm{mm}^3$ polyethylene container filled with an $8\,\mathrm{mm}$ deep layer of distilled water ($100\,\mathrm{cm}^3$). The recipient was cleaned with ethanol and then rinsed with distilled water before each experiment. The distilled water we used was obtained from the Arium pro Ultrapure Water Systems, which, according to the supplier, has a quality superior to the ASTM Type 1 water quality standard.

Vision system. We used an IDS camera USB 3.0 UI-3370CP with the Navitar Lens NMV-75M1 for vision. The camera was configured for a resolution of $1024\,\mathrm{px} \times 1024\,\mathrm{px}$ and the frame rate was $20\,\mathrm{fps}$. The camera was placed at around $80\,\mathrm{cm}$ from the interface, resulting in a field of view of $80 \times 80\,\mathrm{mm}^2$ ($13\,\mathrm{px/mm}$). To be able to accurately identify the objects position from the images, a white back light (PHLOX LEDW-BL-100x-LLUB-Q-1R-24V) was placed below the water recipient to saturate the camera and make it easier to digitally analyze the image. This back light was used when the automatic object detection was necessary, thus explaining the white background in Fig. 3, 4 and 6, but it was not necessary when the laser position was imposed by the user (Fig. 5).

Finally, all the above-described elements, except for the laser and water sources, were placed on top of an anti-vibration table (Newport VH3030W-OPT) to reduce noise during the experiments.

Mirror calibration

To find the adequate mirror rotation to obtain a desired laser position in the camera frame (calibration box in Fig. 2A), a preliminary calibration step is necessary. Since the infrared (IR) laser is not visible to the camera, a visible red laser (Visual Fault Locator TL532) was coupled with the IR laser in the optic fiber using a laser coupler (Thorlabs WD202C-APC). To be able to see the red laser spot, the water recipient was replaced with a white paper surface at approximately the position of the air-water interface. Next, a calibration step, where only the red laser was on, was performed varying the mirror position along both axes and recording the obtained laser spot position in the camera frame. Finally, a third degree 2D polynomial fitting was performed, defining the required mirror position for a desired laser position (calibration box in Fig. 2A). The calibration was also corroborated using the IR laser and a laser viewing card (Thorlabs VIS/NIR Detector Card). The calibration was checked every day before performing experiments, and repeated if necessary.

Software

We wrote a custom C code using the Qt widget toolkit to control the system. We used the provided software development kits to communicate with the camera and the mirror controller. When launched, the software sets the camera configuration and began the image acquisition. Upon the reception of each frame, an image analysis routine based on the OpenCV 2.4.11 was performed. Firstly, the position and orientation of the floating objects were found using the OpenCV contours function. Secondly, a control law routine or the user input was used to determine the desired laser spot position. Thirdly, the previously described mirror calibration was used to find the necessary mirror position that was finally sent to the mirror controller. Each frame, the objects positions, the laser positions, other auxiliary data and, optionally, the received images were saved.

Controlled objects

The spheres shown in Fig.3A had a $0.5\,\mathrm{mm}$ diameter, were made of AISI 420C stainless steel, and were supplied by Redhill Precision. The multiple-legged object shown in Fig. 4A was made using a Digital Light Printing technique operated at the Laboratoire Interdisciplinaire de Physique (LIPhy). The self-assembly parts shown in Fig. 5A and Fig. 6A were made of fused silica, were $0.5\,\mathrm{mm}$ thick, were cut with FEMTOPrint, and were painted with black permanent marker to make them opaque.

Supplementary materials

Text.

Fig. S1: Comparison between ThermoBot and other microrobotic platforms working at the

References

1. A. Barbot, H. Tan, M. Power, F. Seichepine, G.-Z. Yang, Floating magnetic microrobots for fiber functionalization. *Science Robotics* **4**, eaax8336 (2019).

2. A. Pena-Francesch, J. Giltinan, M. Sitti, Multifunctional and biodegradable self-propelled protein motors. *Nature Communications* **10**, 1–10 (2019).

3. F. Ongaro, S. Scheggi, A. Ghosh, A. Denasi, D. H. Gracias, S. Misra, Design, characterization and control of thermally-responsive and magnetically-actuated micro-grippers at the air-water interface. *Plos One* **12**, e0187441 (2017).

4. K. Furukawa, T. Teshima, Y. Ueno, Self-propelled ion gel at air-water interface. *Scientific Reports* **7**, 1–8 (2017).

5. M. Dkhil, M. Kharboutly, A. Bolopion, S. Régnier, M. Gauthier, Closed-loop control of a magnetic particle at the air–liquid interface. *IEEE Transactions on Automation Science and Engineering* **14**, 1387–1399 (2015).

6. M. Mastrangeli, S. Abbasi, C. Varel, C. Van Hoof, J.-P. Celis, K. F. Böhringer, Self-assembly from milli-to nanoscales: methods and applications. *Journal of Micromechanics and Microengineering* **19**, 083001 (2009).

7. Y. S. Song, M. Sitti, Surface-tension-driven biologically inspired water strider robots: Theory and experiments. *IEEE Transactions on Robotics* **23**, 578–589 (2007).

8. X. Zhang, J. Zhao, Q. Zhu, N. Chen, M. Zhang, Q. Pan, Bioinspired aquatic microrobot capable of walking on water surface like a water strider. *ACS Applied Materials & Interfaces* **3**, 2630–2636 (2011).

9. O. Ozcan, H. Wang, J. D. Taylor, M. Sitti, Stride ii: a water strider-inspired miniature robot with circular footpads. *International Journal of Advanced Robotic Systems* **11**, 85 (2014).

10. J. Yan, X. Zhang, J. Zhao, G. Liu, H. Cai, Q. Pan, A miniature surface tension-driven robot using spatially elliptical moving legs to mimic a water strider's locomotion. *Bioinspiration & Biomimetics* **10**, 046016 (2015).

11. G. Lucarini, V. Iacovacci, P. J. Gouveia, L. Ricotti, A. Menciassi, Design of a novel magnetic platform for cell manipulation. *Journal of Micromechanics and Microengineering* **28**, 025009 (2018).

12. T. Yao, N. G. Chisholm, E. B. Steager, K. J. Stebe, Directed assembly and micromanipulation of passive particles at fluid interfaces via capillarity using a magnetic microrobot. *Applied Physics Letters* **116**, 043702 (2020).

13. C. Pawashe, S. Floyd, M. Sitti, Multiple magnetic microrobot control using electrostatic anchoring. *Applied Physics Letters* **94**, 164108 (2009).

14. E. Diller, J. Giltinan, M. Sitti, Independent control of multiple magnetic microrobots in three dimensions. *The International Journal of Robotics Research* **32**, 614–631 (2013).

15. A. Denasi, S. Misra, Independent and leader–follower control for two magnetic microagents. *IEEE Robotics and Automation Letters* **3**, 218–225 (2017).

16. A. Marchand, J. H. Weijs, J. H. Snoeijer, B. Andreotti, Why is surface tension a force parallel to the interface? *American Journal of Physics* **79**, 999–1008 (2011).

17. D. Vella, Floating versus sinking. *Annual Review of Fluid Mechanics* **47**, 115–135 (2015).

18. L. Scriven, C. Sternling, The Marangoni effects. *Nature* **187**, 186–188 (1960).

19. J. W. Bush, D. L. Hu, Walking on water: biolocomotion at the interface. *Annual Review of Fluid Mechanics* **38**, 339–369 (2006).

20. N. Bassik, B. T. Abebe, D. H. Gracias, Solvent driven motion of lithographically fabricated gels. *Langmuir* **24**, 12158–12163 (2008).

21. J. H. Park, S. Lach, K. Polev, S. Granick, B. A. Grzybowski, Metal–organic framework "swimmers" with energy-efficient autonomous motility. *ACS Nano* **11**, 10914–10923 (2017).

22. C. Luo, H. Li, X. Liu, Propulsion of microboats using isopropyl alcohol as a propellant. *Journal of Micromechanics and Microengineering* **18**, 067002 (2008).

23. L. Zhang, Y. Yuan, X. Qiu, T. Zhang, Q. Chen, X. Huang, Marangoni effect-driven motion of miniature robots and generation of electricity on water. *Langmuir* **33**, 12609–12615 (2017).

24. M. A. Rahman, J. Cheng, Z. Wang, A. T. Ohta, Cooperative micromanipulation using the independent actuation of fifty microrobots in parallel. *Scientific Reports* **7**, 1–11 (2017).

25. W. Hu, Q. Fan, A. T. Ohta, An opto-thermocapillary cell micromanipulator. *Lab on a Chip* **13**, 2285–2291 (2013).

26. A. S. Basu, Y. B. Gianchandani, A programmable array for contact-free manipulation of floating droplets on featureless substrates by the modulation of surface tension. *Journal of Microelectromechanical Systems* **18**, 1163–1172 (2009).

27. R. Terrazas, A. Bolopion, J.-C. Beugnot, P. Lambert, M. Gauthier, Closed-loop particle motion control using laser-induced thermocapillary convective flows at the fluid/gas interface at micrometric scale. *IEEE/ASME Transactions on Mechatronics* **23**, 1543-1554 (2018).

28. P. Kralchevsky, V. Paunov, I. Ivanov, K. Nagayama, Capillary meniscus interaction between colloidal particles attached to a liquid—fluid interface. *Journal of Colloid and Interface Science* **151**, 79–94 (1992).

29. D. Vella, P. D. Metcalfe, R. J. Whittaker, Equilibrium conditions for the floating of multiple interfacial objects. *Journal of Fluid Mechanics* **549**, 215–224 (2006).

30. N. Bowden, A. Terfort, J. Carbeck, G. M. Whitesides, Self-assembly of mesoscale objects into ordered two-dimensional arrays. *Science* **276**, 233–235 (1997).

31. M. Poty, G. Lumay, N. Vandewalle, Customizing mesoscale self-assembly with three-dimensional printing. *New Journal of Physics* **16**, 023013 (2014).

32. P. Morin, C. Samson, Motion control of wheeled mobile robots. *Springer Handbook of Robotics* **1**, 799–826 (2008).

33. Dortmund data bank, http://www.ddbst.com. Accessed: 2020-04-15.

34. H. Chraïbi, J.-P. Delville, Thermocapillary flows and interface deformations produced by localized laser heating in confined environment. *Physics of Fluids* **24**, 032102 (2012).

35. J. E. Bertie, Z. Lan, Infrared intensities of liquids xx: The intensity of the oh stretching band of liquid water revisited, and the best current values of the optical constants of h2o (l) at 25 c between 15,000 and 1 cm- 1. *Applied Spectroscopy* **50**, 1047–1057 (1996).

36. E. Lucassen-Reynders, A. Cagna, J. Lucassen, Gibbs elasticity, surface dilational modulus and diffusional relaxation in nonionic surfactant monolayers. *Colloids and Surfaces A: Physicochemical and Engineering Aspects* **186**, 63–72 (2001).

Acknowledgments

We thank Olivier Stephan for the digital light printing of the multiple-legged robots, Sam Dehaeck for providing help with the software and the image analysis algorithm and Ronald Terrazas for the design of the optical system and fruitful discussions on the control laws. **Funding:** This work was funded by BELSPO (IAP 7/38 MicroMAST), FNRS grant (PDR T.0129.18) and the EUR EIPHI program (Contract No. ANR-17-EURE-0002). **Author contributions:** F.P.B performed the flow numerical simulations, developed the ThermoBot dynamic model, implemented the control law for the different objects, and performed the experimental tests. A.B. and M.G. assisted F.P.B. in the development of the control laws, proposed the different experimental tests and supervised the project. P.L. assisted F.P.B. in understanding and modelling the physics of the problem, initiated the project, secured funding, and supervised all steps of the project. **Competing interests:** The authors declare that they have no competing interests. **Data and materials availability:** All data needed to evaluate the conclusions in the paper are present in the paper and/or the supplementary materials.

Supplementary materials

A. Velocity as a function of size and comparison with other air-water actuation methods

See Fig. S1 and Table S1.

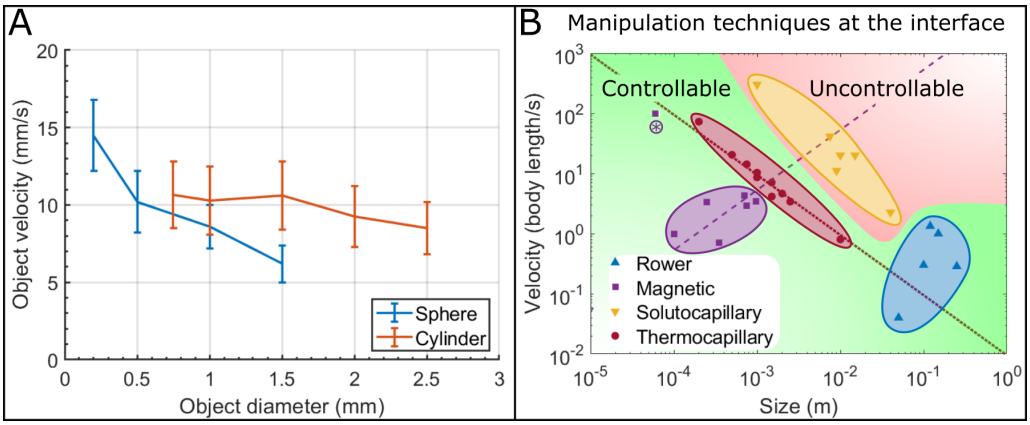

Figure S1: **Comparison between ThermoBot and other microrobotic platforms working at the air-water interface. (A)** Object velocity as a function of diameter for spheres and cylinders with a thickness of $0.5\,\mathrm{mm}$. The measurements correspond to a laser power of $150\,\mathrm{mW}$ and a laser-object distance (center to center) of $1.1\,\mathrm{mm}$. The error bars represent the range (difference between highest and lowest value) of 6 measurements. **(B)** Comparison between rower robots (*7–10*), magnetic actuation (*3, 5, 11, 12*), solutocapillary based actuation (*2, 4, 20–23*), and ThermoBot (measurement shown in (A) and in Fig. 4B). The dashed lines represent the velocity scaling laws (based on the physical principles) of the magnetic actuation and ThermoBot. (*) The speed of this magnetically actuated object (*5*) is obtained over very small distances ($< 300\,\mu\mathrm{m}$).

B. Flow simulations

We performed 2D axisymmetric finite elements simulations using COMSOL Multiphysics 5.5 to estimate the temperature increase, the fluid velocity, its response time, and the range of the effect. We solved the case where a cylindrical volume of water (radius $R_r = 25\,\mathrm{mm}$, height $H_r = 7.5\,\mathrm{mm}$), whose top surface is in contact with air, is heated from above by an infrared laser beam pointed at the center of the water-air interface (Fig. 2B). For the used wavelength ($\lambda = 1455\,\mathrm{nm}$), water is opaque and the absorbed power per unit volume is (*34*)

$$\dot{q_L} = \frac{2P_L\alpha}{\pi {R_L}^2} \exp\left(-2\left(\frac{r}{R_L}\right)^2 + \alpha\,(H_r - z)\right) \tag{S1}$$

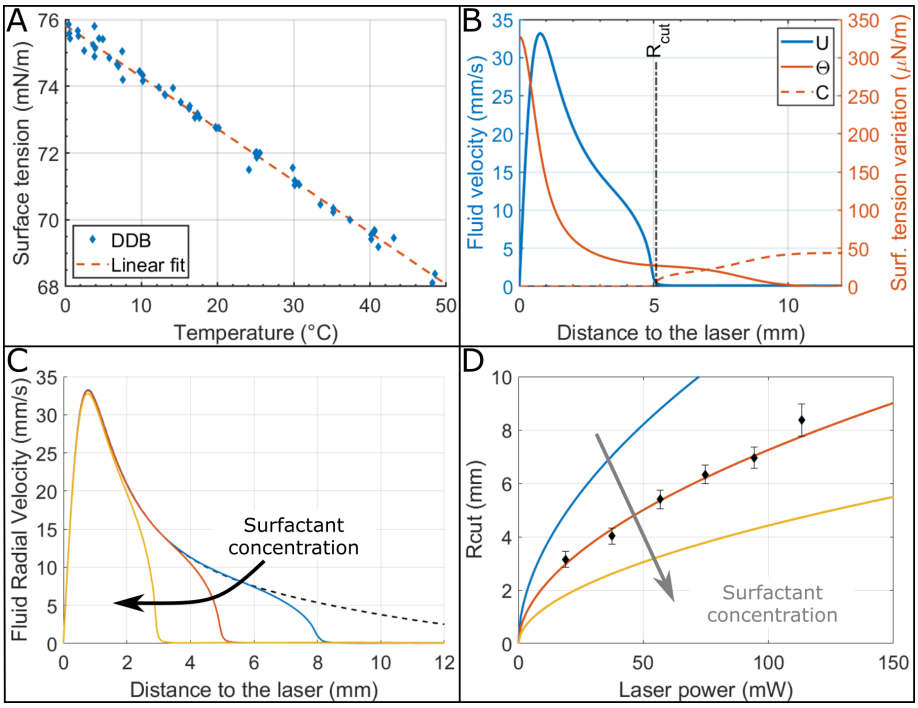

Figure S2: **Thermocapillary flow simulation.** **(A)** Surface tension variation with the temperature (data obtained from the Dortmund Data Bank (*33*)) and its linear fit $\sigma = 72.7\,\mathrm{mN/m} - 155\,\mu\mathrm{N/(m\,K)}\,(T - 20\,^\circ\mathrm{C})$. **(B)** Surface flow simulation results for a laser power of $50\,\mathrm{mW}$ and $(\partial\sigma/\partial\Gamma)\,\Gamma_0 = 40\,\mu\mathrm{N/m}$ where $\Theta = (\partial\sigma/\partial T)(T - T_0)$ and $C = (\partial\sigma/\partial\Gamma)\Gamma$. **(C)** Surfactant concentration effect on the surface velocity for the same laser power as B. It mainly affects the size of the convection cell (R_{cut}) while the maximum flow velocity remains almost constant. The dashed line represents the no surfactant case (infinite range) and the solid ones represent the cases $(\partial\sigma/\partial\Gamma)\,\Gamma_0 = 20\,\mu\mathrm{N/m}$, $40\,\mu\mathrm{N/m}$ and $80\,\mu\mathrm{N/m}$. **(D)** Variation of R_{cut} as a function of the laser power for the same surfactant concentrations as C and measurements performed by spreading aluminum flakes (typical size of $70\,\mu\mathrm{m}$) on the interface and measuring how far they are repelled by the flow. The error bars represent the range (difference between highest and lowest value) of 3 measurements.

Table S1: Comparison between rower robots (*7–10*), magnetic actuation (*3, 5, 11, 12*), solutocapillary-based actuation (*2, 4, 20–23*), and ThermoBot actuation.

Technique	**Control**	**Objects**	**Miniaturization**	**Workspace limits**	**Lifespan limits**
Rower	Individual	Onboard actuators	Difficult	Only for tethered case	Only for non-tethered case
Magnetic	Global	Magnetic material	Yes	Magnetic field range	None
Solutocapillary	No	Containing fuel	Yes	None	Fuel depletion and surface saturation
ThermoBot	Individual	Any floating object	Yes	Mirror rotation limits	None

where the laser divergence is neglected (collimated beam), P_L is the laser power, $R_L = 0.65\,\mathrm{mm}$ is the laser radius, $\alpha = 3280\,\mathrm{m}^{-1}$ is the absorption coefficient per unit length (*35*), r is the radial coordinate and z is the vertical coordinate (origin at the bottom of the recipient). For this geometry, Eq. (1) can be expressed as the boundary condition

$$\mu \left(\left. \frac{\partial u}{\partial z} \right|_{z=H_r} = \frac{\partial \sigma}{\partial T} \left(\left. \frac{\partial T}{\partial r} \right|_{z=H_r} \right. \right. \tag{S2}$$

where u is the radial velocity and $\partial\sigma/\partial T = 155\,\mu\mathrm{N}/(\mathrm{m\,K})$ in our temperature range (Fig. S2A). This boundary condition links the temperature with the momentum equation. The standard mass, momentum, and energy conservation equations together with Eqs. (S1) and (S2) correctly describe the phenomena close to the laser spot ($r < 2\,\mathrm{mm}$). These equations allowed us to obtain the results shown in Fig. 2C, but they predicted an infinite convection cell in the radial direction (infinite range) which did not agree with our experimental observations. To solve this discrepancy, it was necessary to consider the surface elasticity (*36*) produced by uncontrolled surfactants that get adsorbed at the interface. Qualitatively, before turning on the laser there is a homogeneous layer of surfactants adsorbed at the air-water interface that slightly reduce the surface tension. When the laser is turned on and the thermocapillary flow begins to develop, it conveys the surfactants away, creating a depletion around the laser spot and thus increasing the surface tension, and counteracting the effect of the temperature. At a given distance from the laser spot (that we call R_{cut}), this effect completely compensates the temperature gradient and thus stops the convection cell from growing any further. This was simulated by adding to Eq. (S2) the surfactant's effect

$$\mu \left(\left. \frac{\partial u}{\partial z} \right|_{z=H_r} = \frac{\partial \sigma}{\partial T} \left(\left. \frac{\partial T}{\partial r} \right|_{z=H_r} + \frac{\partial \sigma}{\partial \Gamma} \frac{\partial \Gamma}{\partial r} \right. \right. \tag{S3}$$

where Γ is the superficial surfactant concentration. This new boundary condition, together with the standard transport equation for the surfactant, allows us to match the experimental

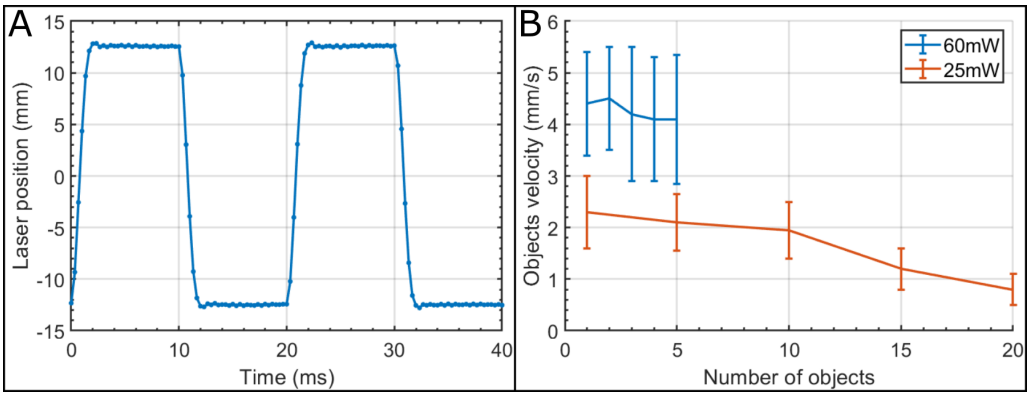

Figure S3: **Laser multiplexing.** **(A)** Laser spot positions response to square wave reference command. Measurement done using a high-speed camera and the visible red laser. **(B)** Sphere velocity as a function of the number of particles keeping a constant local laser power (total laser power divided by the number of particles) and a laser-particle distance of $1.1\,\mathrm{mm}$. The blue line ($60\,\mathrm{mW}$ local laser power) was obtained by displacing simultaneously the corresponding number of particles, while the orange one ($25\,\mathrm{mW}$ local laser power) was obtained by displacing three particles simultaneously and the rest were simulated by placing the laser in the corner of the workspace during the corresponding time. The error bars represent the range (difference between highest and lowest value) of the different particles' velocities during one single measurement.

observations adjusting the initial surfactant concentration to $(\partial\sigma/\partial\Gamma)\,\Gamma_0 \approx 40\,\mu\mathrm{N/m}$. With this new model, the flow takes the shape of a finite toroidal convection cell (Fig. 2B) and we see that from a given distance (R_{cut}) the surfactant concentration gradient completely compensates the temperature gradient (Fig. S2B). The initial concentration of surfactants determines the size of the convection cell (Fig. S2C) and how it grows with the laser power (Fig. S2D). For small concentrations it does not strongly affect the maximum fluid velocity, but high enough concentrations would completely stop the thermocapillary flow.

C. Laser multiplexing

We used a high-speed camera and the visible red laser to observe how the laser spot is displaced by the mirror. When we commanded the mirror to switch continuously between two positions (reference square signal), we observed that it takes the mirror around $2\,\mathrm{ms}$ to displace the laser from one spot to the other (Fig. S3A), independently of the distance between them. Taking this into account, whenever we want to multiplex the laser between several spots, we command it to stay $10\,\mathrm{ms}$ at each spot, which would results in the laser staying $8\,\mathrm{ms}$ and expending the other $2\,\mathrm{ms}$ traveling between points (wasting $20\,\%$ of the laser power). This wasted power could have an effect on the floating objects (much lower than the effect of the spots) that could be avoided by adding a shutter to the setup that would block the laser while rotating the mirror. On the other

hand, our previously described numerical simulations allowed us to estimate the fluid response time to be around $50\,\mathrm{ms}$ (it varies with the laser power) at a distance of $1\,\mathrm{mm}$ from the laser spot (the distance of the peak fluid velocity). At longer distances, this response time becomes larger. Taking this into account, when multiplexing the laser, it should not expend more than $50\,\mathrm{ms}$ away from each spot to avoid the fluid velocity decreasing too much, thus limiting the number of spots to around five. We measured the velocity of multiple spheres being controlled simultaneously as a function of the number of spheres keeping the local laser power (total laser power divided by number of spots) constant and we observed that the velocity remains almost constant if the number is less than five, but then it starts to decrease (Fig. S3B).

D. Sphere model and control

We developed a simplified model of the system which consisted in defining a steady state velocity ($\mathbf{U_{SS}}$) as a function of the laser position relative to the sphere. This steady state velocity is the velocity the sphere would attain if the relative laser position were kept constant (Fig. 3B) and its direction is given by the laser-sphere direction. To consider the fluid and sphere inertia, a time constant τ was added

$$\dot{\mathbf{U}} = \frac{\mathbf{U_{SS}} - \mathbf{U}}{\tau} \tag{S4}$$

where $\mathbf{U}$ is the sphere velocity. This model is geometrically illustrated in Fig. S4A. We estimated $\tau \approx 0.2\,\mathrm{s}$ using the transitory data for the $500\,\mu\mathrm{m}$ diameter steel spheres (Fig. S4B). We developed two different control laws: one for the path following and another for the tracking. For the path-following case (Fig. 3D), the control law was designed neglecting the sphere dynamics (we assumed $\mathbf{U} = \mathbf{U_{SS}}$). Firstly, we found the closest point of the path to the sphere and calculated the path orientation (θ_P) and curvature (κ_P) at this point, as well as the sphere-path distance (d_p). Then, we decoupled the velocity magnitude and orientation control. Since we wanted to slow down at high curvature zones, the desired velocity magnitude is given by

$$U_d = \frac{U_{\max}}{1 + A1\,\kappa_P} \tag{S5}$$

where $U_{\max} = 5.4\,\mathrm{mm/s}$ and $A1 = 3\,\mathrm{mm}$. On the other hand, to make the sphere stay on the path, we defined a returning angle as

$$\theta_e = -\arctan\left(\frac{d_P}{A2}\right) \tag{S6}$$

where $A2 = 1\,\mathrm{mm}$. Therefore, the desired movement direction will be $\theta_d = \theta_P + \theta_e$. Finally, the laser spot was moved to the position that would generate the desired velocity magnitude and orientation. Simulations using our control law and the described model taking into account the sphere dynamics show that, after the initial approach, the distance to the path should be kept under $0.5\,\mathrm{mm}$ (Fig. S4C), which is consistent with our experimental results (Fig. 3C) considering the simplicity of the model.

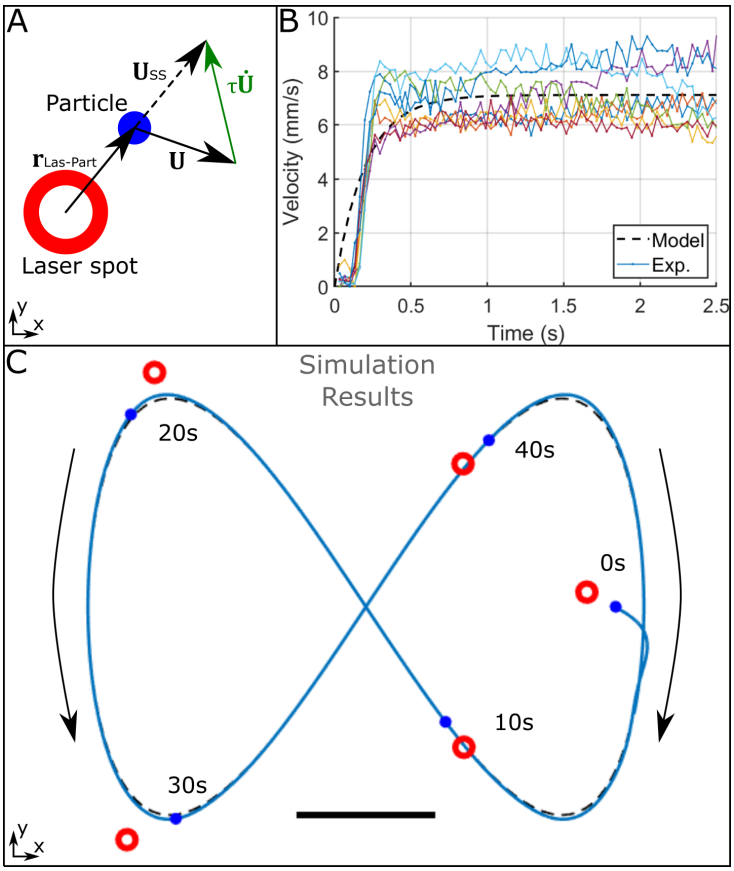

Figure S4: **Sphere model and control simulation.** **(A)** Schematics of Eq. (S4) relating the particle acceleration ($\dot{\mathbf{U}}$) to the difference between the steady state velocity corresponding to the given laser position ($\mathbf{U_{SS}}$) and the particle velocity ($\mathbf{U}$) through a time constant (τ), modelling the liquid and particle inertia. **(B)** Experimental fitting of the time constant $\tau = 0.2\,\mathrm{s}$ using the transitory measurements obtained for a laser power of $75\,\mathrm{mW}$ and keeping a laser-sphere distance of $1.1\,\mathrm{mm}$. **(C)** Simulation results with the designed controller. The blue and red circles represent the sphere and laser spot respectively at different times. The dashed line represents the commanded path and the solid one, the resultant trajectory. Scale bar $10\,\mathrm{mm}$.

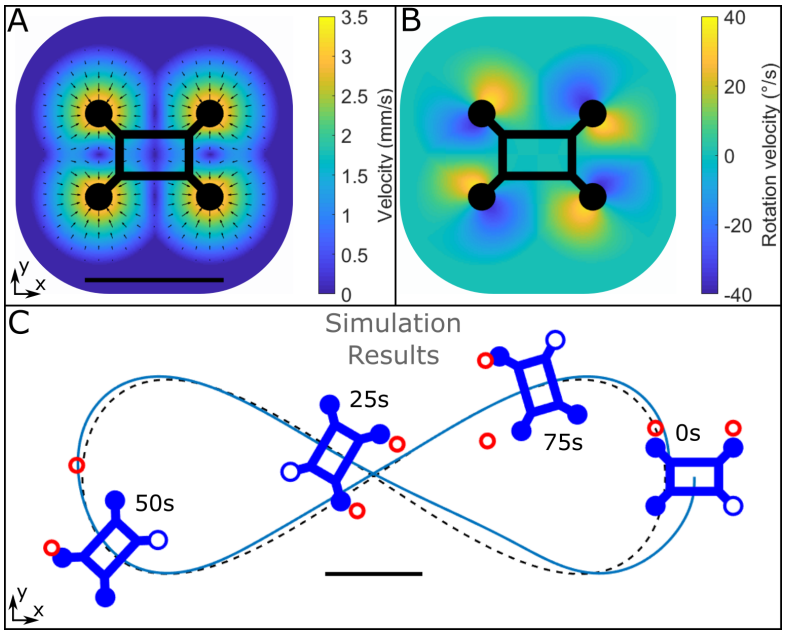

Figure S5: **Multiple-legged object model and control simulation.** **(A)** Representation of the steady velocity (magnitude and orientation) that a laser spot would induce on the object if the relative position is kept constant. Result for a laser power of $150\,\mathrm{mW}$. Scale bar $10\,\mathrm{mm}$. **(B)** Similar to A but with the rotation velocity. Same laser power and scale as A. **(C)** Simulation results with the designed controller and the developed model. The blue figures and red circles represent the object and laser spot respectively at different times. The dashed line represents the commanded path and the solid one, the resultant trajectory. Scale bar $10\,\mathrm{mm}$.

As for the tracking (Fig. 3E), a simpler control law was implemented neglecting the target movements and the sphere dynamics. Firstly, the sphere-target distance d_T and orientation θ_T are calculated. Secondly, the desired movement direction is computed towards the target position ($\theta_d = \theta_T$) and the velocity magnitude as

$$U_d = U_{\max}\left(1 - \exp\left(-\frac{d_T}{A3}\right)\right) \tag{S7}$$

where $U_{\max} = 5.4\,\mathrm{mm/s}$ and $A3 = 2\,\mathrm{mm}$. Finally, the laser spot is moved to the position that will generate the desired velocity magnitude and orientation, unless the distance to the target is less than $0.25\,\mathrm{mm}$, distance that we consider acceptable, in which case the laser is removed.

E. Multiple-legged object model and control

Similarly, a model was developed for the object with four legs. In this case, we use Eq. (S1) with an estimated $\tau \approx 1\,\mathrm{s}$ on each leg to obtain the corresponding acceleration and then the

total linear and angular accelerations of the center of mass was computed. The steady velocity magnitude and direction for a single laser spot as a function of its position are illustrated in Fig. S5A. The same was done with the steady rotation velocity in Fig. S5B. Assuming that the effect of multiple laser spots corresponds to the addition of each one's effect (assumption observed to be valid if the laser spots are sufficiently apart from each other), the model parameters were estimated using the experimental data (Fig. 4B). According to our model, if we put both laser spots at different distances $d1$ and $d2$ from their respective legs, we observe that the advancement speed mainly depends on the average distance $D_A = (d1 + d2)/2$ while the rotation curvature ($K_R = \omega/U$) mainly depends on the difference between the two distances $D_R = (d1 - d2)$.

In the path-following experiment (Fig. 4D), we tried to minimize the robot-path distance and to keep the object orientation (θ_R) aligned with the path orientation. In this case, the system results to be nonholonomic (*32*) and the controller had to be designed accordingly. Firstly, we found the closest point of the path to the object and calculated the path orientation (θ_P), curvature (κ_P) and curvature derivative ($\dot{\kappa_P}$) at this point, the robot-path distance (d_P), and finally the orientation error ($\theta_e = \theta_R - \theta_P$). Secondly, since in our experiment we controlled the rotation curvature ($K_R = \omega/U$), we adapted the coordinate transformation given in (*32*) to avoid the velocity estimation defining the variables:

$$Z = (1 - \kappa_P d_P) \tan\theta_e \tag{S8}$$

$$V1 = \frac{\cos\theta_e}{1 - \kappa_P d_P} \tag{S9}$$

$$V2 = \frac{(K_R - \kappa_P V1)\left((1 + \kappa_P d_P)^2 + Z^2\right) - (\kappa_P Z + \dot{\kappa_P} d_P) Z\, V1}{(1 - \kappa_P d_P)}. \tag{S10}$$

The control law is given by

$$V2 = -B1\, V1\, d_P - B2\, |V1|\, Z \tag{S11}$$

where B1=0.5 and B2=$3\,\mathrm{mm}$. Finally, the control consists in using Eqs. (S8) and (S9) to compute Z and $V1$ respectively, then using Eq. (S11) to find $V2$ and, finally, solving Eq. (S10) to obtain K_R. We use the value of K_R to determine the value of D_R. In this experiment, we did not implement a slow down for the high curvature areas but, since a minimum laser-leg distance of $1\,\mathrm{mm}$ was kept, D_A was automatically increased when D_R was high enough. Simulations using our control law and model showed that, after the initial approach, the distance to the path should be kept under $1\,\mathrm{mm}$ (Fig. S5C), which underestimates the experimental error (Fig. 4C). This could be explained by the fact that the implemented controller is sensitive to disturbances (e.g. water droplets on the object changing the mass distribution, a foot being more immersed than the others due to fabrication errors, etc.). Moreover, most of the object remains above the water surface, being exposed to air currents.

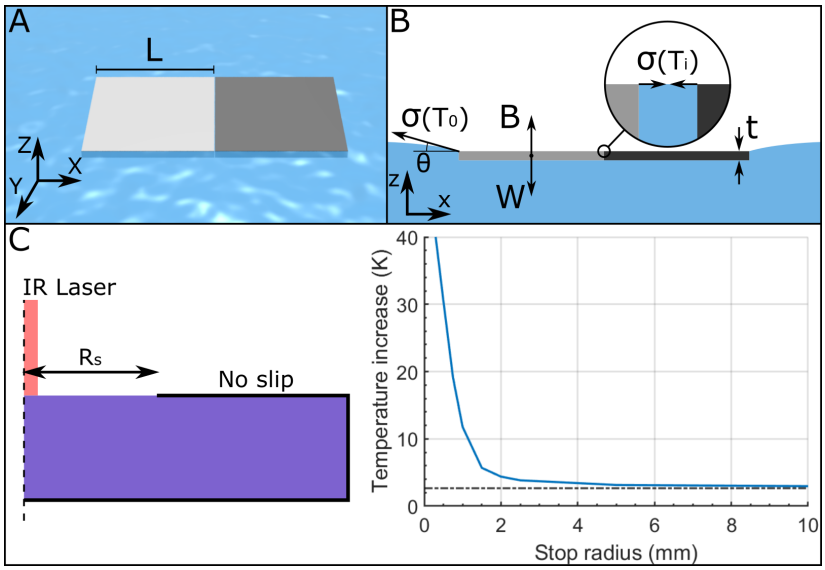

Figure S6: **Forces acting on self-assembled objects and their separation.** **(A)** Two floating square objects kept together by lateral capillary forces. **(B)** Free body diagram and forces acting on each particle. There are three forces, the surface tension forces (σ), the weight (W), and the buoyancy (B). **(C)** Simulation results (Supplementary Material B) for a laser power of $75\,\mathrm{mW}$ without surfactants when a no slip boundary condition was imposed at the interface for a radius higher than a stop radius (R_S). We consider an adiabatic boundary condition on the top surface, but for a high temperature increase the energy transferred to the air may become non-negligible. The dashed line represents the result shown in Fig. 2C.

F. Separation of assembled particles using the laser

In this section, we present our hypothesis explaining the assembly pieces separation using the laser. To simplify the analysis, we will assume two floating square objects with a side length of $L = 8\,\mathrm{mm}$ and a thickness of $t = 0.5\,\mathrm{mm}$ (similar to the pieces shown in Fig. 5) kept together by capillary forces (Fig. S6A). There are three forces acting on each particle, the surface tension, the weight, and the buoyancy force (Fig. S6B). Between the objects, the contact will not be perfect due to the objects' roughness and it will be limited to some contact points. Therefore, there will still be pockets of fluid between the objects. The interface between the objects will be almost horizontal and the force pulling the objects towards each other (attraction) will be $F_a = L\,\sigma$ where σ is the surface tension. On the other side, the interface will have an angle θ with respect to the horizontal plane, therefore the force pulling the objects away from each other (repulsive) will be $F_r = L\,\sigma\,\cos(\theta)$. We conclude that if the surface tension is homogeneous, then $F_a > F_r$ and the objects will stay together. From a vertical forces point of view and assuming a homogeneous surface tension and θ around the two particles, we obtain

$$6L\,\sigma\sin(\theta) < 2gL^2e\,(\rho_s - \rho_l) \tag{S12}$$

where ρ_s and ρ_l are the object and liquid densities respectively and g is the gravity acceleration. The inequality results from the fact that the buoyancy force would be higher than the volume of the object times the liquid density times the gravity acceleration because of the interface deformation and the increased liquid pressure below the object (*17*). Assuming $\rho_s = 2200\,\mathrm{kg/m^3}$ (the density of fused silica), $\rho_l = 1000\,\mathrm{kg/m^3}$ and $\sigma = 72\,\mathrm{mN/m}$, we obtain $\theta < 13°$. Assuming this limit value as the actual value of θ, the net attractive force results $F = F_a - F_r = L\,\sigma\,(1 - \cos(\theta)) \approx 15\,\mu\mathrm{N}$. If we place the laser between the objects, the temperature would increase and the surface tension between the pieces would decrease: $\sigma = \sigma_0 - \gamma_T \Delta T$. Assuming that the temperature around the particles does not increase, the net attractive force would be

$$F = L\,(\sigma_0\,(1 - \cos(\theta)) - \gamma_T \Delta T) \tag{S13}$$

and it would become negative (turn repulsive) if $\Delta T > \sigma_0/\gamma_T\,(1 - \cos(\theta)) \approx 12\,\mathrm{K}$. Therefore, we conclude that a temperature increase larger than $12\,\mathrm{K}$ is enough to separate the pieces. Such a temperature increase can easily be obtained using the infrared laser since in this case there is no flow (Fig. S6C). Moreover, if the pieces are not perfectly in contact, the developed thermocapillary flow would also help separate the pieces.